1

Combining Optical Transparency with Electrical Conductivity: Challenges and Prospects

Julia E. Medvedeva

Department of Physics, Missouri University of Science and Technology, USA

1.1 Introduction

Transparent conductors are neither 100% optically transparent nor metallically conductive. From the band structure point of view, the combination of the two properties in the same material is contradictory: a transparent material is an insulator which possesses completely filled valence and empty conduction bands; whereas metallic conductivity appears when the Fermi level lies within a band with a large density of states to provide high carrier concentration.

Efficient transparent conductors find their niche in a compromise between a sufficient transmission within the visible spectral range and a moderate but useful in practice electrical conductivity [1–6]. This combination is achieved in several commonly used oxides – In_2O_3, SnO_2, ZnO and CdO. In the undoped stoichiometric state, these materials are insulators with optical band gap of about 3 eV. To become a transparent conducting oxide (TCO), these TCO hosts must be degenerately doped to displace the Fermi level up into the conduction band.

The key attribute of any conventional n-type TCO host is a highly dispersed single free-electron-like conduction band [7–13] (Figure 1.1). Degenerate doping then provides both (i) the high mobility of extra carriers (electrons) due to their small effective mass and (ii) low optical absorption due to the low density of states in the conduction band. The high energy dispersion of the conduction band also ensures a pronounced Fermi energy

Transparent Electronics: From Synthesis to Applications Edited by Antonio Facchetti and Tobin J. Marks

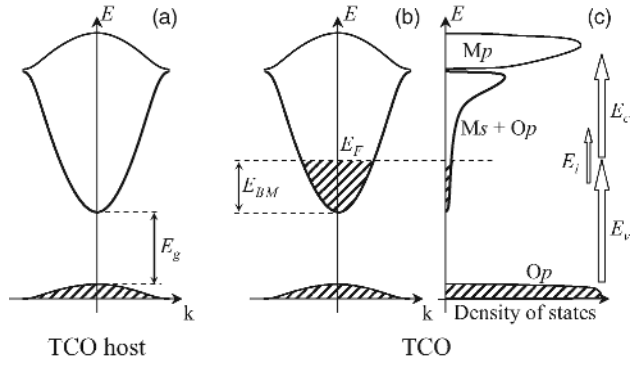

Figure 1.1 *(a) Schematic electronic band structure of a TCO host – an insulator with a band gap E_g and a dispersed parabolic conduction band which originates from interactions between metal s and oxygen p states. (b) and (c) Schematic band structure and density of states of a TCO, where a degenerate doping displaces the Fermi level (E_F) via a Burstein-Moss shift, E_{BM}, making the system conducting. The shift gives rise to inter-band optical transitions from the valence band, E_v, and from the partially filled conduction band up into the next empty band, E_c, as well as to intra-band transitions within the conduction band, E_i*

displacement up above the conduction band minimum, the Burstein–Moss (BM) shift [14, 15]. The shift helps to broaden the optical transparency window and to keep the intense optical transitions from the valence band out of the visible range. This is critical in oxides which are not transparent throughout the entire visible spectrum, for example, in CdO where the optical (direct) band gap is 2.3 eV.

Achieving the optimal performance in a TCO is a challenging because of the complex interplay between the electronic and optical properties [16, 17]. The large carrier concentrations desired for a good conductivity may result in an increase of the optical absorption [18] (i) at short wavelengths, due to inter-band transitions from the partially filled conduction band and (ii) at long wavelengths, due to intra-band transitions within this band. In addition, plasma oscillations may affect the optical properties by reflecting the electromagnetic waves of frequency below that of the plasmon. Furthermore, ionized impurity scattering on the electron donors (native point defects or substitutional dopants) have a detrimental effect on the charge transport, while the structural relaxation around the impurities may alter the electronic and optical properties of the host, leading to a nonrigid-band shift of the Fermi level.

This chapter is devoted to *ab initio* electronic band structure investigations of common TCOs and related oxide materials. We demonstrate here that a thorough understanding of the microscopic properties of metal oxides provides an insight into the underlying phenomena and also suggests that the range of efficient TCO materials can be significantly broadened.

1.2 Electronic Properties of Conventional TCO Hosts

Conventional n-type TCO hosts (In_2O_3, SnO_2, CdO and ZnO) share similar chemical, structural and electronic properties. Exclusively oxides of the post-transition metals with

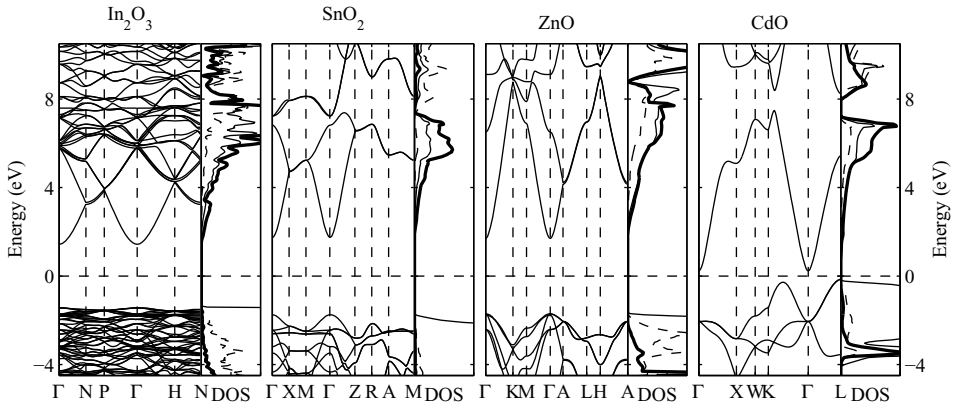

Figure 1.2 *Electronic band structure and partial density of states of TCO hosts, In_2O_3, SnO_2, ZnO and CdO, as obtained within the screened-exchange local-density approximation [19]. In the density of states plots, the thick, dashed and thin lines represent metal s, metal p and oxygen p states, respectively. The plots should be compared with the schematic band structure shown in Figure 1.1(a)*

$(n-1)d^{10}ns^2$ electronic configurations, they have densely packed structures with four- or six-coordinate metal ions. Strong interactions between the oxygen 2*p* and metal *ns* orbitals give rise to electronic band structures qualitatively similar for all these oxides (cf. Figures 1.1 and 1.2): the bonding and nonbonding O 2*p* states form the valence band while the conduction band arises from the antibonding M*s*–O*p* interactions. The empty *p* states of the metal ion form the following band at a higher energy. The partial density of states plots (Figure 1.2), reveal that the oxygen 2*p* and metal *ns* states make similar contributions to the conduction band. This provides a three-dimensional M*s*–O*p* network for charge transport once extra carriers fill the band.

M*s*–O*p* interactions result in a gap between the valence and the conduction bands. In ZnO, the gap is direct whereas in CdO, In_2O_3 or SnO_2 the valence band maximum is at the L point ([111]), H point ([$1\bar{1}1$]) or R point ([011]), respectively, giving rise to an indirect band gap of 0.4 eV, 2.6 eV or 2.7 eV, respectively. Table 1.1 lists the direct optical

Table 1.1 *Basic properties of conventional TCO hosts. The optical band gaps and the electron effective masses are determined within screened-exchange local-density approximation (sX-LDA) [19]. Anisotropy of the electron effective mass is defined as* $\delta = (m^{[100]} + m^{[010]})/2m^{[001]}$

Oxide	Lattice	Coordination of		Optical (direct) band gap (eV)	Electron effective mass, m_e			Effective mass anisotropy
		cation	anion		$m^{[100]}$	$m^{[010]}$	$m^{[001]}$	
ZnO	Wurtzite	4	4	3.41	0.35	0.35	0.35	1.008
CdO	Rocksalt	6	6	2.28	0.23	0.23	0.23	1.000
In_2O_3	Byxbyite	6	4	3.38	0.28	0.28	0.28	1.000
SnO_2	Rutile	6	3	3.50	0.33	0.33	0.28	1.179

band gaps which are of primary importance for TCO applications. These values are obtained from the electronic band structure calculations within screened-exchange local density approximation (sX-LDA) [19], which gives good agreement with the reported experimental values (3.5–3.7 eV for In_2O_3, 2.3 eV for CdO, 3.1–3.6 eV for ZnO and 3.6–4.0 eV for SnO_2) [25–29].

The M*s*–O*p* overlap also determines the energy dispersion of the conduction band in these materials. Within the framework of $\mathbf{k}\cdot\mathbf{p}$ theory [30], the electron effective mass can be found within the second-order perturbation:

$$\frac{m_e}{m_{ii}^{(c)}} = 1 + \frac{2}{m_e}\sum_{l\neq c}\frac{|\langle u^{(c)}|\hat{p}_i|u^{(l)}\rangle|^2}{E^{(c)}-E^{(l)}}, \tag{1.1}$$

where p is the momentum operator, $|u^{(l)}\rangle$ is the Bloch wave function of the l's band at the Γ point (wave vector $\mathbf{k}=0$) and $E^{(l)}$ is its energy. Band label c represents the conduction band, while the sum runs over all other bands. In the oxides under consideration here, the electron effective mass is less than the mass of the electron, m_e. As it follows from Equation (1.1), it is determined primarily by the valence band contributions ($E^{(l)} < E^{(c)}$), i.e. by the oxygen 2*p* states.

From the orbital symmetry considerations (Figure 1.3) coordination of cations *by the oxygen atoms* have little effect on the M*s*–O*p* overlap owing to the spherical symmetry of the *s* orbitals. The largest M*s*–O*p* overlap is attained when the oxygen atom is coordinated octahedrally *by the cations*, i.e. when each of the oxygen p_x, p_y and p_z orbitals connects two *s* orbitals (Figure 1.3). Accordingly, the octahedral coordination of the oxygen atoms in rocksalt CdO gives rise to the largest dispersion and, hence, the smallest electron effective mass among the TCO materials (Table 1.1). However, it was found [31] that variations in the oxygen coordination and strong distortions in the polyhedra have little effect on the electron effective mass which varies insignificantly when the symmetry of the same-cation oxide

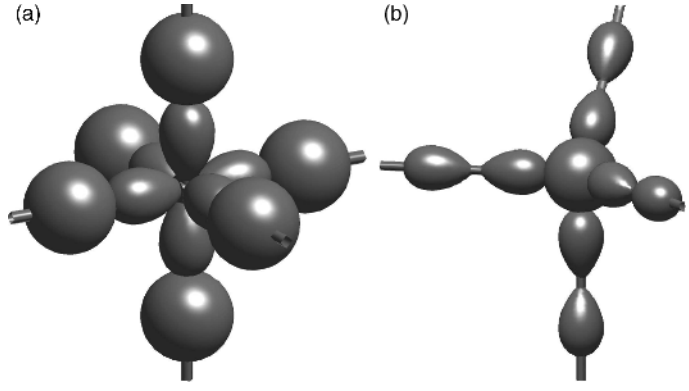

Figure 1.3 *Octahedral coordination of oxygen atoms by cations (a) provides the largest overlap between the oxygen p_x, p_y and p_z orbitals and the s orbitals of the metal ions. Coordination of cations by oxygen atoms as well as local distortions (b) have little effect on the Ms–Op overlap owing to the spherical symmetry of the metal s orbitals*

is changed. For example, for ZnO in rocksalt (octahedral coordination) or wurtzite (tetrahedral coordination) structures, and for In_2O_3 in $Ia\bar{3}$ (byxbyite), $R\bar{3}c$ (corundum) or $I2_13$ structures, the effective masses vary by about 15%. Moreover, the effective mass remains nearly isotropic in all phases of the oxides – including those with irregular atomic arrangements or large structural voids [31, 32].

Little sensitivity of the M*s*–O*p* overlap and, hence, of the electron effective mass to structural variations may explain the success of amorphous TCOs whose optical and electrical properties remain similar to those in the crystalline state [6, 33–37]. This is in marked contrast to, for example, amorphous Si where the directional interactions between the conduction *p* orbitals lead to strong anisotropy of the transport properties which are sensitive to the orbital overlap and, hence, to the distortions in the atomic chains [36].

Thus, the network of alternating metal and oxygen atoms ensures the small electron effective mass in the TCO hosts. A direct overlap between metal *s* orbitals is not possible in these materials except for SnO_2 where Sn atoms may bond along the edge-sharing rutile chain (along the [001] crystallographic direction). However, the fact that the calculated [11, 31] (Table 1.1) and the observed [38] electron effective mass in this oxide is nearly isotropic suggests that the *s*–*s* interactions do not govern the transport properties of TCOs.

In the next section, where we will consider the conversion of the TCO hosts from insulators to conductors, the M*s*–O*p* origin of the conduction band will play a critical role.

1.3 Carrier Generation in Conventional TCO Hosts

The optical and transport properties of a conventional TCO are governed by the efficiency and the specifics of the carrier generation mechanism employed. Even in the most favorable situation, i.e. when the effects of dopant solubility, clustering, secondary phase formation and charge compensation can be avoided, large concentrations of electron donors (substitutional dopants and/or native point defects) not only promote the charge scattering but also may significantly alter the electronic band structure of the host oxide, leading to a nonrigid-band shift of the Fermi level. A detailed band structure analysis of the doped oxides helps to elucidate the role of different factors involved.

1.3.1 Substitutional Doping

Substitutional doping with aliovalent ions is the most widely used approach to generate free carriers in TCO hosts. Compared with native point defects, it allows a better control over the resulting optical and transport properties as well as better environmental stability of the TCO films. Traditionally, same-period, next-row elements, e.g, Sn^{4+} for In^{3+} and In^{3+} for Cd^{2+}, are thought to provide better compatibility and, thus, less disturbance in the host crystal and electronic structure. However, other dopants may prove beneficial for optimizing the properties for a specific application. For example, transparent conducting ZnO films have been prepared by doping with Group III (Al, Ga, In and B), Group IV (Si, Ge, Ti, Zr and Hf) and a Group VII element (F substituted at an oxygen site), giving rise to a wide range of electrical conductivities [39].

Here we will give a detailed consideration to rocksalt CdO, where the high crystal symmetry and the densely packed structure ensures the most uniform charge density distribution via the isotropic M*s*–O*p* network. Compared with more complex In_2O_3 or SnO_2, one can expect fewer ionized and neutral scattering centers and, hence, longer relaxation times. At the same time, introduction of dopants into the densely packed structure may significantly influence the Cd*s*–O2*p* hybridization and, therefore, alter the structural, electronic and optical properties of the host. A systematic comparison of CdO doped with In, Ga, Sc or Y, whose ionic radius and electronic configuration differ from those of the host cation, has revealed [40–42] that:

(i) Substitutional dopants with smaller ionic radii compared with that of Cd shrink the lattice. The shrinkage, however, is not as large as expected from the Vegard's law weighted average [43] of the six-coordinated X^{3+} and Cd^{2+} ionic radii. Moreover, in the case of X = In or Y, the lattice parameter is similar or even slightly greater than that of CdO (cf. Table 1.2). One of the possible explanations is that the doping-induced shrinkage is compensated by an expansion mechanism which originates from the antibonding character of the conduction band formed from Cd 5*s* and O 2*p* states [44, 45]. The antibonding mechanism is dominant in In or Y doped CdO, while Sc or Ga have sufficiently smaller ionic radii to weaken M*s*–O*p* hybridization and, thus, to compress the lattice.

(ii) Weaker Cd5*s*–O2*p* hybridization associated with strong structural relaxation around dopant with a smaller ionic radius results in a smaller optical band gap (cf. Table 1.2). Doping with Ga whose ionic radius is significantly smaller than that of Cd, reduces the optical band gap (to 2.53 eV) so that it becomes smaller than the one in undoped CdO (2.82 eV) – despite the doping-introduced BM shift of 2.3 eV. The smallest optical

Table 1.2 *Properties of 12.5 at% doped CdO as obtained from electronic band structure calculations within the screened-exchange local-density approximation [40–42]. Dopant X^{3+}, where X = Y, In, Sc or Ga, substitutes Cd^{2+} (ionic radius 1.09 Å), while F^- substitutes O^{2-} atoms. The electron velocity is calculated in the [100](Δ), [110](Σ) and [111](Λ) directions. Values for CdO with one extra electron ($CdO + e^-$) are found from a rigid band shift. Reprinted with permission from [41]. Copyright 2005 American Chemical Society*

	e^-	Y	In	Sc	Ga	F
Dopant ionic radius (Å)	–	1.04	0.94	0.89	0.76	1.19
Lattice parameter (Å)	4.66	4.67	4.66	4.63	4.62	4.65
Distance X-O or Cd-F (Å)	–	2.28	2.24	2.18	2.08	2.38
Distance Cd-O (Å)	2.33	2.39	2.42	2.45	2.54	2.27
Optical band gap (transitions E_v) (eV)	4.56	3.38	3.03	3.02	2.53	2.73
Optical transitions E_c (eV)	8.30	0.70	0.51	0.83	0.94	0.73
Fundamental band gap (eV)	2.82	2.99	2.54	3.13	2.42	2.64
Hybridization gap (eV)	0.95	–	–	0.55	0.65	–
Band width (eV)	7.29	3.36	3.91	2.57	3.01	4.17
Electron velocity, v^{Δ} ($\times 10^5$ m s^{-1})	10.39	9.12	10.54	4.65	8.25	9.45
v^{Σ} ($\times 10^5$ m s^{-1})	10.43	9.61	10.29	7.66	7.46	10.24
v^{Λ} ($\times 10^5$ m s^{-1})	9.43	9.17	9.23	7.95	2.94	9.36
Density of states at the Fermi level	0.96	1.34	1.16	2.00	1.74	1.21

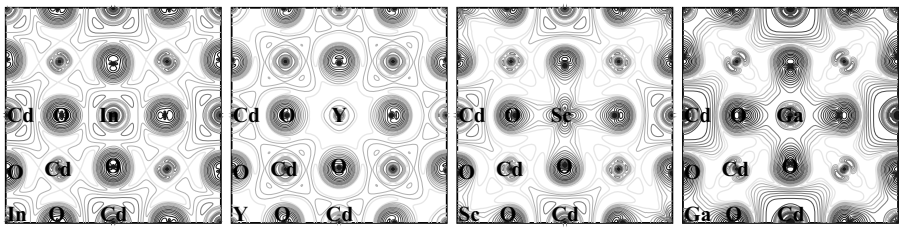

Figure 1.4 *Contour plots of the charge density distribution in In, Y, Sc and Ga-doped CdO illustrate considerable electron localization around Sc and Ga ions as compared with In and Y cases where the charge density is more uniform. The plots are calculated in the xy plane within the 2kT energy window near the Fermi level. The grey scale increases with charge; the same scale is used for all plots. Atoms within one unit cell are labeled. Reprinted with permission from [41]. Copyright 2005 American Chemical Society*

band gap in Ga-doped CdO as compared with In, Y and Sc cases was observed experimentally [40–42].

(iii) In and Y dopants preserve the uniform charge density distribution while Sc and Ga lead to significant electron localization around the dopant (Figure 1.4). The difference originates from the mismatch of the electronic configuration of the dopants and the energy location of the dopant empty *p* or *d* states with respect to the Fermi level. The Sc 3*d* states and Ga 4*p* states are energetically compatible with the conduction 5*s* states of Cd, while the Y 4*d* and In 5*p* are located higher in energy. As a result, the contributions from the Sc *d* or Ga *p* orbitals become significant near the Fermi level: the Sc *d* orbital contribution is dominant (85% of the Sc total) and the Ga *p* and *s* orbitals give comparable contributions (60% and 40%, respectively). The anisotropic Sc *d* or Ga *p* orbitals form strong directional bonds with the orbitals of the nearest oxygen atoms resulting in significant charge localization which is clearly seen from the charge density distribution plots (Figure 1.4).

(iv) The electron localization in Sc and Ga doped CdO results in a narrower conduction band and, hence, a reduction of the electron velocity as compared with In or Y (Table 1.2). Moreover, due to the high anisotropy of the Sc *d* or Ga *p* orbitals, a significantly reduced velocity is found in the Δ (Sc *d* orbitals) or Λ (Ga *p* orbitals) directions so that anisotropic transport properties are expected.

(v) The electron binding in Sc and Ga-doped CdO also leads to larger (in energy) optical transitions from the Fermi level (E_c in Figure 1.1), in contrast to the In and Y cases where the charge delocalization deminishes the second (hybridization) gap.

(vi) Finally, we note that even in the In, Y and F cases where the dopant ionic radius and electronic configuration are similar to that of Cd or O, the optical properties are worse than expected from the rigid band shift ($CdO + e^-$) (Table 1.2). However, the calculated electron velocity and the density of states for In, Y and F-doped CdO are similar to those obtained from the rigid-band model (Table 1.2). Both factors contribute to the conductivity σ, given by the expression:

$$\sigma = \frac{2e^2}{\Omega} \sum_{\mathbf{k}\lambda} |v_{\mathbf{k}\lambda}|^2 \tau_{\mathbf{k}\lambda} \delta(E_{\mathbf{k}\lambda} - E_F), \tag{1.2}$$

so that the relaxation time τ will play the dominat role in determining the final carrier transport. [In Equation (1.2) e is the electron charge, Ω is the volume of the Brillouin zone, $\mathbf{k}$ is the wave vector, λ is the band index, v is the electron group velocity and E_F is the Fermi energy.] Assuming that τ is similar for all X^{3+}-doped systems, estimates of the Fermi electron velocity and the density of states at the Fermi level result in the trend In > Y > Sc > Ga, which is in agreement with experimental observations of the conductivity [40–42].

1.3.2 Oxygen Reduction

Removal of an oxygen atom from a metal oxide leaves two extra electrons in the crystal. Whether one or both of these electrons become free carriers or remain localized at the vacancy site correlates with the oxide free energy of formation. In light metal oxides, such as CaO or Al_2O_3, where the formation energy is high, oxygen vacancies create deep charge-localized states within the electronic band gap known as color or F centers. A relatively low formation energy of the conventional TCOs [46] favors large oxygen deficiencies even under equilibrium growth conditions, giving rise to the free-carrier densities of 10^{17}–10^{19} cm^{-3} for In_2O_3 and ZnO [47–49].

Electronic band structure investigations of oxygen deficient oxides [49–51] showed that the oxygen defect $V_O^{\bullet\bullet}$ (in Kröger–Vink notation the superscript $^\bullet$ stands for effective positive charge) corresponds to a nonconducting state associated with the filling of the lowest single conduction band by the two vacancy-induced electrons. Only if the vacancy is excited, e.g. via a photoexcitation [49], or partially compensated to $V_O^{\bullet}$, does the single conduction band become half-occupied and conducting behavior may occur.

In oxygen deficient TCOs, the conduction band wave function resembles the one in the corresponding hosts [50, 52], i.e. it is derived from the M *s* and O *p* states (Figure 1.1). A relatively uniform charge density distribution suggests that the vacancy-induced electrons are delocalized [52]. However, a more thorough analysis of reduced In_2O_3 reveals [50] that the metal atoms nearest to the oxygen defect give about two times larger contributions than the rest of the In atoms in the cell. As a result, there is a notable build-up of the charge density near the vacancy site. Importantly, the In atoms nearest the vacancy exhibit a reduction of the *s*-orbital contribution: the relative orbital contributions from the In *s*, *p* and *d* states are 81%, 8% and 11%, respectivly, in contrast to 97% *s*-orbital contributions from other In atoms in the cell. The high anisotropy of the *p* and *d* orbitals favors stronger covalent (directional) bonds between the In atoms which surround the defect and their oxygen neighbors. These In–O pairs trap about 31% of the total charge density at the bottom of the conduction band. Similar behavior is found for other TCOs: in oxygen deficient CdO and ZnO, 18% and 39%, respectively, of the total charge density belong to the nearest (cation) and next nearest (oxygen) neighbors of the oxygen vacancy [50].

The presence of oxygen vacancies leads to significant changes in the electronic band structure of a TCO host. To illustrate the typical behavior, we compare the results obtained for oxygen deficient and Sn-doped In_2O_3 (cf. Table 1.3 and Figure 1.5):

(i) Strong structural relaxation around the vacancy reduces the distance between the In and O atoms nearest to the defect to 2.12 Å (on average). This leads to an increased In–O distances for the atoms located further from the defect and, hence, to a weaker

Table 1.3 *Properties of oxygen-deficient and Sn-doped In_2O_3 as obtained from electronic band structure calculations within local density approximation. Values for undoped stoichiometric In_2O_3 found from a rigid band shift are given for comparison. The electron concentration is 1.95×10^{21} cm^{-3} for all systems. The plasma frequency is calculated from Equation (1.3)*

	Optical transitions (eV)		Fundamental band gap (eV)	Plasma frequency (eV)	Electron velocity ($\times 10^5$ m s^{-1})			$N(E_F)$
	E_v	E_c			$v^{[001]}$	$v^{[111]}$	$v^{[1\bar{1}1]}$	
$In_2O_3 + e^-$	3.01	0.54	1.16	2.35	9.42	9.45	8.60	1.51
$In_2O_3 + Sn^{\bullet}_{In}$	2.72	0.71	0.98	2.25	8.93	9.17	8.66	1.73
$In_2O_3 + V^{\bullet}_{O}$	2.07	1.11	0.71	1.32	5.58	6.42	4.81	3.36

In*s*–O*p* hybridization. As a result, the fundamental band gap and the optical transitions from the valence band (E_v) are significantly reduced in oxygen-deficient In_2O_3 as compared with Sn-doped oxide.

(ii) Owing to the stronger binding between the In and O atoms nearest to the defect, the lowest single conduction state occupied by the vacancy-induced electrons is split from the rest of the conduction band by a second gap. In marked contrast, the second gap is absent in the substitutionally doped oxide. This is a manifestation of a more uniform spatial charge density distribution, i.e. the charge delocalization. Note, the second gap previously reported for Sn-doped In_2O_3 [9] vanishes upon structural relaxation around Sn ions [cf. Figure 1.5(b)].

(iii) The increased charge density in the vicinity of the oxygen vacancy and the related narrowing of the conduction band give rise to the reduced electron velocity (Table 1.3). At the same time, the density of states near the Fermi level increases. Since both factors contribute to the conductivity [cf. Equation (1.2)], the difference in the charge

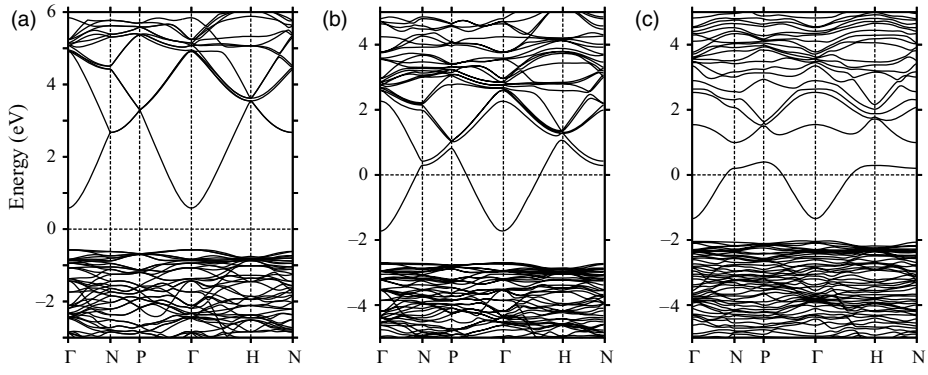

Figure 1.5 *Electronic band structure of (a) undoped stoichiometric In_2O_3. Reprinted with permission from [13]. Copyright (2007) Springer Science + Business Media (b) 6.25 at% Sn-doped In_2O_3 and (c) oxygen-deficient In_2O_3 as obtained within the local density approximation [19]. Reprinted with permission from [54]. Copyright (2006) American Physical Society*

transport of the oxygen-deficient and Sn-doped In_2O_3 will be determined primarily by the relaxation time τ in the same equation. Qualitatively, the stronger structural relaxation with the atomic displacements around the oxygen vacancy being twice as large as those around Sn ions [50], implies a stronger charge scattering in oxygen-deficient oxide. In addition, a shorter electron relaxation time in this case should be expected due to the Coulomb attraction of the free carriers to $V_O^{\bullet}$ associated with its higher formation energy compared with that of $V_O^{\bullet\bullet}$, which is the ground-state defect [49]. Moreover, due to the strong preference of the extra electrons to bind with $V_O^{\bullet}$ to form $V_O^{\bullet\bullet}$, the charge transport will be adversely affected since the latter defect corresponds to a nonconducting state [49, 50] (a completely filled single conduction band).

(iv) Due to the narrower conduction band in the oxygen-deficient oxide, the plasma frequency is expected to be significantly smaller than that in Sn-doped material. The plasma oscillations affect the optical properties: the electromagnetic waves of frequency below (and wavelength above) ω_p are reflected due to the electron screening. The plasma frequency is given by the expression:

$$\omega_p^2 = \frac{8\pi e^2}{3\Omega} \sum_{\mathbf{k}\lambda} |v_{\mathbf{k}\lambda}|^2 \delta(E_{\mathbf{k}\lambda} - E_F), \tag{1.3}$$

where e is the electron charge, Ω is the volume of the Brillouin zone, $\mathbf{k}$ is the wave vector, λ is the band index, v is the electron group velocity and E_F is the Fermi energy. Our estimates for ω_p in the oxygen-reduced and Sn-doped In_2O_3 as well as the one obtained from the rigid band model are given in Table 1.3.

In summary, compared with substitutional doping, oxygen reduction of a TCO host may result in higher carrier densities but would limit the electron mobility due to shorter relaxation times and considerable charge trapping near the vacancy site. Also, a weaker M*s*–O*p* hybridization due to stronger structural relaxation around the vacancy significantly reduces the optical transparency window.

There may be other native point defects that give rise to a conducting behavior in a TCO. For example, it was shown that interstitial Sn ions in SnO_2 have low formation energies and produce donor levels inside the conduction band of this material [53]. In this case, significant structural rearrangement associated with the formation of Sn(II)O bonds as in SnO [53] is expected to have an even stronger effect on the properties of the oxide host and to increase electron scattering.

The above considerations demonstrate the advantages of employing substitutional doping as a primary carrier generation mechanism in conventional TCO hosts. However, notwithstanding the above limitations, we believe that varying the degree of nonstoichiometry may serve as a versatile tool for optimizing a TCO's overall performance.

1.4 Magnetically Mediated TCO

Transition metal dopants opened up an avenue for alternative carrier generation in conventional TCO hosts [54]. Initially, carrier mobility with more than twice the value

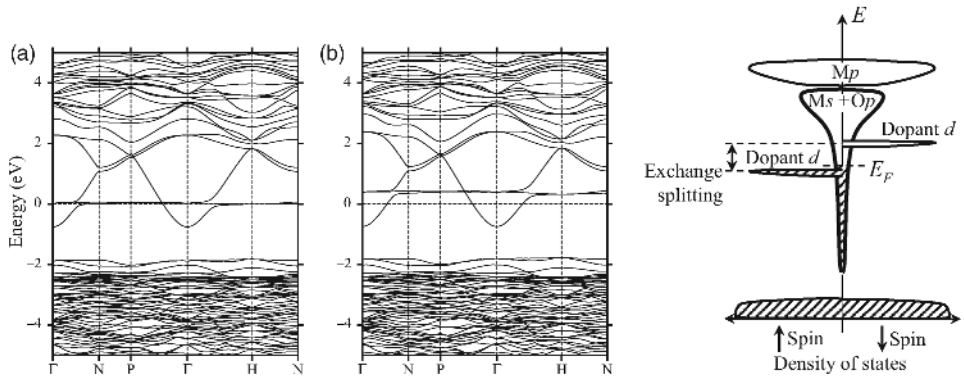

Figure 1.6 *Electronic band structure for (a) the majority and (b) the minority spin channels of 6.25% Mo-doped In_2O_3 compensated with an oxygen vacancy. In (c), the results of (a) and (b) are shown schematically. Reprinted with permission from [13, 54]. Copyright (2007) Springer Science + Business Media; Copyright (2006) by the American Physical Society*

of the commercial Sn-doped indium oxide (ITO) was observed in Mo-doped In_2O_3 (IMO), and the resulting enhanced conductivity appeared with no changes in the spectral transmittance upon doping with Mo [55–57]. Surprisingly, introduction of the transition metal Mo^{6+} which is expected to donate two more carriers per substitution compared with Sn^{4+}, does not lead to the expected increase of the optical absorption or a decrease of the mobility due to the scattering on the localized Mo *d* states.

Electronic band structure investigations of IMO revealed [54] that both high carrier mobility and low optical absorption originate from the Mo-induced magnetic interactions. Strong exchange interactions split the Mo *d* states so that the occupied *d* states with spin up lie just below the Fermi level while the empty spin down *d* states are well above it (Figure 1.6). The partial density of states suggests that in the majority spin channel about 58% of the total density near the Fermi level comes from the Mo *d* states while the rest is spread uniformly throughout the cell. In the minority spin channel, contributions from the Mo *d* states at the Fermi level are negligible and the conduction charge density distribution resembles that in In_2O_3. Therefore, the spin-up *d* states are resonant states, while the charge transport occurs through the In*s*–O*p* network. In other words, the free carriers in the system flow in a background of the Mo defects which serve as scattering centers. As a result of the exchange splitting of the Mo *d* states, the carriers of one spin are affected by only a half of the scattering centers, i.e. only by the Mo *d* states of the same spin. Therefore, the concentration of the Mo scattering centers is effectively lowered by half compared with the Mo doping level. The lack of long-range magnetic order leads to the formation of two interpenetrating networks transporting efficiently the carriers of opposite spin.

Significantly, the BM shift is less pronounced in the IMO case – despite the fact that Mo^{6+} donates two extra carriers as compared with Sn^{4+} at the same doping level. Such a low sensitivity to doping appears from the resonant Mo *d* states located at the Fermi level that facilitates the *d*-band filling (pinning) and thus hinders further displacement of the Fermi

level deep into the conduction band. The smaller BM shift in IMO leads to the following advantageous features to be compared with those of ITO:

(i) Smaller increase in the electron effective mass with respect to the value in undoped stoichiometric In_2O_3 is expected upon Mo doping. This is borne out in experimental observations [56] showing that the effective mass does not vary with doping (up to 12% of Mo) and carrier concentration.
(ii) Larger (in energy) optical transitions from the partially occupied band (E_c in Figure 1.1) ensure lower short-wavelength optical absorption.
(iii) The calculated plasma frequency, ω_p, in IMO (1.3 for $[Mo_{In}^{\bullet\bullet\bullet} O''_i]^{\bullet}$ and 1.6 eV for $Mo_{In}^{\bullet\bullet\bullet}$ defects) is significantly smaller than that of ITO (2.3 eV). This finding suggests the possibility to introduce larger carrier concentrations without sacrificing the optical transmittance in the long wavelength range.

It should be pointed out that smaller BM shift in IMO does not lead to the appearance of the intense inter-band transitions from the valence band, E_v, in the visible range due to the large optical band gap in pure indium oxide (3.4 eV). Furthermore, in contrast to ITO where the band gap narrowing has been demonstrated both experimentally [26] and theoretically [9], the fundamental band gap of IMO was found to increase upon introduction of Mo [54].

The properties of IMO can be further optimized by varying ambient oxygen pressure [57]. An increased oxygen content in IMO facilitates the formation of the oxygen compensated complexes, e.g. $[Mo_{In}^{\bullet\bullet\bullet} + 2In_{In} O''_i]^{\bullet}$ or $[Mo_{In}^{\bullet\bullet\bullet} O''_i]^{\bullet}$, where the subscript stands for the site position and the superscript stands for effective negative ($'$) or positive ($^{\bullet}$) charge. These complexes reduce the number of free carriers – from three to one per Mo substitution – but, at the same time, enhance the carrier mobility due to smaller ionized impurity scattering and, hence, longer relaxation times. However, the interstitial oxygen significantly supresses the magnetic interactions which should be strong enough to split the transition metal *d* states in order to provide good conductivity in one (or both) spin channels [54].

In summary, we have shown that transition metal dopants offer the possibility to enhance conductivity via an increased mobility (due to smaller BM shift) of the free carriers and not their concentration (since half of the carriers are trapped on the *d* states of Mo). The latter usually leads to reduction of the optical transparency.

The advantages of carrier generation via *d*-element doping will be also discussed in Section 1.7.

1.5 Multicomponent TCO Hosts

Multicomponent TCOs, complex oxides which contain a combination of In, Zn, Cd and Sn metal ions, have been developed to broaden the range of the TCO materials required for a variety of specialized applications. Binary and ternary compounds and solid solutions with electrical, optical and mechanical properties controlled via chemical composition, have been the subject of numerous investigations [1, 2, 4, 58–60]. Since the 1990s, multi-cation TCOs which include metal ions beyond the traditional Sn, Cd, In and Zn have emerged. For example, $MgIn_2O_4$ [61], $GaInO_3$ [62] and Ga_2O_3-containing 2-3-3 or 3-3-4 systems, where

Table 1.4 *Net contributions to the conduction band at the Γ point from the states of the atoms that belong to the $InO_{1.5}$ layer, N_1, or $Ga(Al)Zn(Cd,Mg)O_{2.5}$ layers, N_2, in per cent; the electron effective masses m, in m_e, along the specified crystallographic directions; and the components of the electron effective-mass tensor, m_{ab} and m_z, calculated via simple averaging of those of the corresponding single-cation oxides [Equations (1.6) and (1.7)]. Reprinted with permission from [13, 31]. Copyright (2007) Springer Science + Business Media and (2007) Institute of Physics Publishing respectively*

Compound	N_1 (%)	N_2 (%)	$m_{[100]}$	$m_{[010]}$	$m_{[001]}$	m_{ab}	m_z
$InGaZnO_4$	48	52	0.23	0.22	0.20	0.23	0.23
$InAlCdO_4$	54	46	0.26	0.25	0.20	0.27	0.27
$InGaMgO_4$	58	42	0.27	0.27	0.24	0.28	0.29
$InAlMgO_4$	72	28	0.32	0.31	0.35	0.31	0.34

the numbers correspond to divalent, trivalent and tetravalent cations [8], have attracted wide attention.

Electronic band structure investigations [31, 50] of multi-cation oxides with layered structures [63–69], $InGaZnO_4$, $InAlCdO_4$, $InGaMgO_4$ and $InAlMgO_4$, identified the key electronic feature of complex oxides – the hybrid nature of the conduction band associated with the strong hybridization between the states of *every* cation in the cell with the states of its neighboring oxygen atoms. Strikingly, despite the substantially different values of the band gaps in the constituent single-cation oxides (e.g. the band gap of Al_2O_3 and MgO is about two times larger than the one in In_2O_3, CdO and ZnO), the states of all cations were found to have comparable contributions to the bottom of the conduction band of the multicomponent oxides (Table 1.4 and Figure 1.7). This results in a uniform three-dimensional charge density distribution within and across the structurally and chemically distinct layers (Figure 1.7) as well as in isotropic electron effective mass (Table 1.4).

Moreover, because the states of all cations contribute to the bottom of the conduction band, the electron effective mass of the complex oxides is an 'effective' average over the effective masses of the single-cation constituents. This averaging can be shown analytically within the tight-binding approximation. A one-dimensional chain consisting of two types of metal atoms which alternate with oxygen atoms (Figure 1.8) captures the key features of complex oxides. The Hamiltonian for such model system where nearest-neighbor interactions are given by the hopping integrals β_1 and β_2, is:

$$H = \sum_{n,l} |n,l\rangle \varepsilon_l \langle n,l| + \sum_{n,n',l,l'} |n',l'\rangle \beta_l \langle n,l|. \tag{1.4}$$

Here l is the atom index in the unit cell, n enumerates the cells and n', l' is the second sum run over the nearest neighbors. For the bottom of the conduction band, the dispersion relation can be simplified to:

$$\varepsilon(\mathbf{k}) = \frac{\varepsilon_1 + \varepsilon_2}{2} + \frac{1}{\frac{1}{2}\left(\frac{\Delta}{\beta_1^2} + \frac{\Delta}{\beta_2^2}\right)} (\mathbf{k}a)^2 \tag{1.5}$$

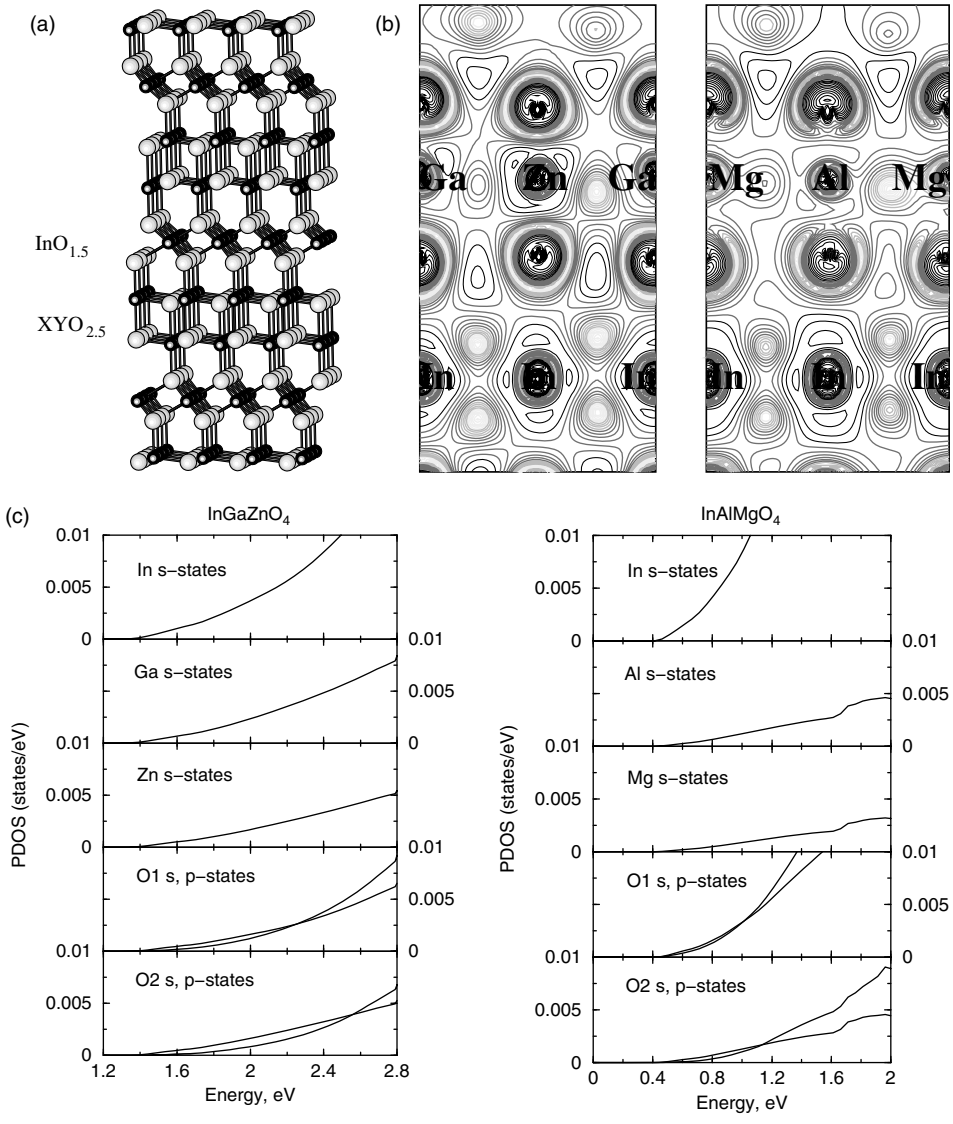

Figure 1.7 *(a) The unit cell of $InXYO_4$ (X = Ga, Al and Y = Zn, Cd, Mg) has three similar blocks, each consisting of one $InO_{1.5}$ layer with octahedral oxygen coordination of In atoms and a double layer $XYO_{2.5}$ with tetrahedral oxygen coordination of the cations. The layers alternate along the [0001] direction. The X^{3+} and Y^{2+} atoms are distributed randomly. (b) Contour plots of the charge density distribution calculated in the (011) plane for the conduction band in $InGaZnO_4$ and $InAlMgO_4$ with extra electron concentration of $\sim 1 \times 10^{18}\,cm^{-3}$. The uniform interatomic charge density distribution within and across the chemically and structurally distinct layers implies isotropic electron transport. (c) Partial density of states at the bottom of the conduction band of $InGaZnO_4$ and $InAlMgO_4$. Although the contributions from Al s and Mg s states are notably reduced, these states will participate in charge transport once the electrons fill the band. Reproduced from [13, 31] by permission of Europhysics Letters Assiciation and of Springer Science + Business Media*

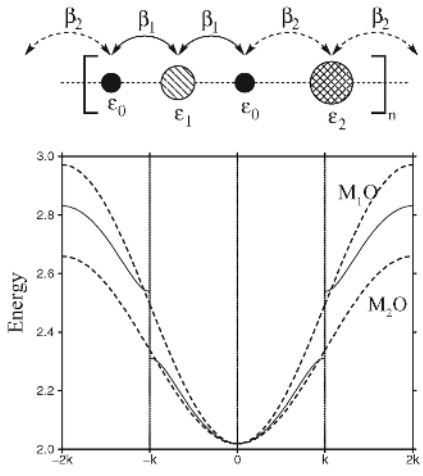

Figure 1.8 *Tight-binding conduction band (solid line) calculated for one-dimensional atomic chain depicted above the plot. Two types of metal atoms (\ and × filled cirles) alternate with oxygen atoms (filled circles) and only the nearest-neighbor hopping β is assumed. To illustrate the effective mass averaging, the conduction bands for the corresponding single-metal oxide chains (dashed lines) are aligned with $(\varepsilon_1+\varepsilon_2)/2$. The following parameters were used: $\varepsilon_0 = 1.00$, $\varepsilon_1 = 2.00$, $\varepsilon_2 = 2.05$, $\beta_1 = 0.4$ and $\beta_2 = 0.5$. Reproduced with permission from [31]. Copyright (2007) Institute of Physics*

if $|\varepsilon_1 - \varepsilon_2| < 2\frac{\beta_1^2-\beta_2^2}{\Delta}$. Here ε_0, ε_1 and ε_2 are the atomic level energies of the oxygen and two types of metal atoms, respectively, and it is assumed that $\varepsilon_0 < \varepsilon_{1,2}$ and $\varepsilon_1 \sim \varepsilon_2$; $\Delta = \frac{1}{2}(\varepsilon_1+\varepsilon_2)-\varepsilon_0$ and a is half of the lattice parameter. Similar considerations for the chain consisting of only one type of metal atom alternating with oxygen atoms show that the quantity $\frac{\Delta}{\beta^2}$ represents the effective mass of that system. Therefore, Equation (1.5) represents the effective mass averaging over those in the corresponding single-metal 'oxide' chains (Figure 1.8).

First-principle calculations confirm the results found in the tight-binding model. For the layered oxides, the effective mass can be estimated as follows. As the resistivity along the z direction, i.e. across the layers, is a sum of the resistivities of each layer, the z component of the average effective-mass tensor can be found as:

$$m_z = (m_1 + m_2 + m_3)/3, \tag{1.6}$$

where $m_{1,2,3}$ are the effective masses of the corresponding single metal oxides, e.g. In_2O_3, Ga_2O_3 and ZnO in the case of $InGaZnO_4$. For the in-plane charge transport, the effective-mass tensor components can be found in a parallel manner:

$$\frac{1}{m_{a,b}} = \frac{1}{3}\left[\frac{1}{m_1} + \frac{2}{\frac{1}{2}(m_2+m_3)}\right]. \tag{1.7}$$

Here, one needs to average the effective mass for the mixed $GaZnO_{2.5}$ layers (Figure 1.7). The obtained $m_{a,b}$ and m_z values nearly coincide with the corresponding calculated effective masses of the multi-cation oxides.

The above effective-mass averaging procedure can be generalized for materials consisting of any number of layers, e.g. for $InGaO_3(ZnO)_m$, where m is an integer. Moreover, because the intrinsic transport properties are determined by the M*s*–O*p* interactions which show little sensitivity to the oxygen coordination and the distortions in the metal-oxygen chains (as discussed earlier), the effective mass averaging should also apply to the oxides in amorphous state. In this case, one needs to average the components of the effective-mass tensor, $m_{\text{amorph}} = (m_a + m_b + m_z)/3$.

Thus, similar to the single-cation TCO hosts, multicomponent oxides have the conduction band formed from M *s* and O *p* states. Nonetheless, no multicomponent oxide has outperformed the conventional single-cation TCOs, in part due to challenges of carrier generation. Targeted doping via aliovalent substitution becomes difficult as the number of multivalent cations increases owing to a possibility of same-valence substitution or anti-site defects [8] which can neutralize the donors. The effects of clustering and second phase formation narrow the range of dopants efficient for a particular multicomponent oxide even further. In addition, the isotropic electronic properties may not be maintained due to a nonuniform distribution of carrier donors in the complex TCO hosts with structural anisotropy, e.g. atomic layers or chains of edge-sharing polyhedron in spinels. For example, preferential distribution of oxygen vacancies as well as Sn, Ti and Zr dopants in $InGaZnO_4$ [50] explains the observed strong anisotropy of the electrical conductivity in $InGaO_3(ZnO)_m$ compounds where the number of ZnO layers is increased [63, 64].

We note that many of these carrier generation bottlenecks may be overcome in the amorphous state of these complex oxides which represents a more uniform mixture of the constituent oxides while preserving the short range structure (alternating metal and oxygen atoms) and, thus, an even stronger hybridization between the states of the different cations mediated by their interactions with the states of shared oxygen atoms. Experimental observations that the mobility and conductivity are independent of the large variations in the composition in amorphous [65] but not in crystalline [8] $InGaO_3(ZnO)_n$ with $n \leq 4$, support the above idea.

Studies [31] of multi-cation TCOs which include light metal ions, such as Al and Mg, motivate an intruguing question: how do these ions influence carrier generation and the resulting transport properties of the multicomponent oxides? Furthermore, we also would like to understand why transparent conducting behavior is unique to SnO_2, In_2O_3, CdO and ZnO but has not been attained in SiO_2, Al_2O_3, CaO or MgO. To address these questions, we will first look at the electronic structure of classic insulators, CaO and Al_2O_3, to determine the origin of the strong electron localization in these oxides.

1.6 Electronic Properties of Light Metal Oxides

Oxides of light metals, such as CaO, MgO, Al_2O_3 or SiO_2, have the same s^2 valence electron configuration of the cations as the conventional TCOs and, therefore, their electronic band structure is similar to the one in a TCO host (cf. Figures 1.1, 1.2 and

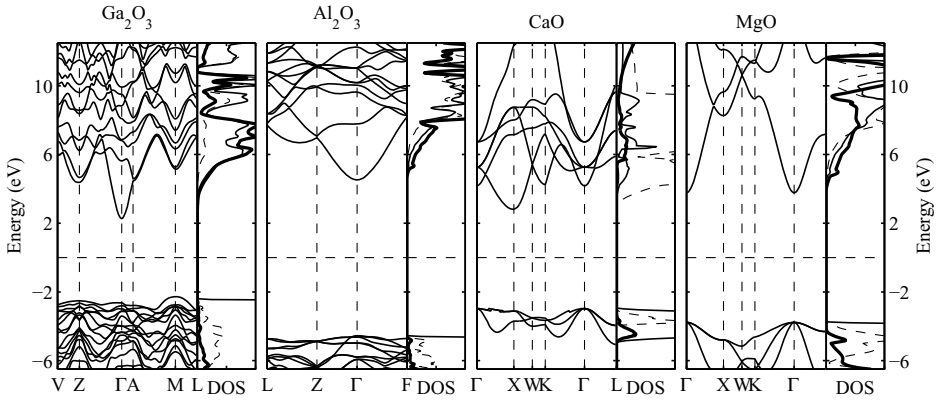

Figure 1.9 *Electronic band structure and partial density of states of several main group metal oxides, Ga_2O_3, Al_2O_3, CaO and MgO, as obtained within the screened-exchange local-density approximation [19]. In the density of states plots, the thick, dashed and thin lines represent metal s, metal p and oxygen p states, respectively*

Figure 1.9). It features a dispersed conduction band resulting in a relatively small electron effective mass of 0.3–0.5 m_e [31] (Table 1.5). However, degenerate doping of these refractory oxides has been a challenge [70–72]. Natural defects, e.g. oxygen vacancy, create deep charge-localized states within the electronic band gap, known as color or F centers.

Electronic band structure investigations of oxygen-deficient MgO, CaO and Al_2O_3 [51] demonstrate the strong localization of the vacancy-induced electrons near the oxygen vacancy – even despite the large concentration of defects used in the calculations, $\sim 0.8–1.0 \times 10^{21}$ cm^{-3}. For these oxides, about 80–87% of the total charge density at the bottom of the conduction band resides at the metal and oxygen atoms which are nearest to the defect. Further analysis reveals large contributions from the Mg *p* states (47%), Ca *d* states (56%) or Al *p* states (47%) while their *s* states contribute only 20–30% to the total

Table 1.5 *Properties of several main group metal oxides. The optical band gaps and the electron effective masses are determined within the screened-exchange local-density approximation (sX-LDA) [24]. The anisotropy of the electron effective mass is defined as* $\delta = (m^{[100]} + m^{[010]})/2m^{[001]}$

Oxide	Lattice	Coordination of		Optical (direct) band gap (eV)	Electron effective mass, m_e			Effective mass anisotropy
		cation	anion		$m^{[100]}$	$m^{[010]}$	$m^{[001]}$	
β-Ga_2O_3	Monoclinic	6,4	4,3	4.86	0.35	0.35	0.32	1.097
Al_2O_3	Corundum	6	4	9.08	0.45	0.45	0.45	1.000
CaO	Rocksalt	6	6	7.15	0.42	0.42	0.42	1.000
MgO	Rocksalt	6	6	7.55	0.46	0.46	0.46	1.000

Table 1.6 *Origin of the electron localization in oxides of main group metals. The larger the p and d orbital contributions on the cations nearest the oxygen vacancy, the more charge is localized near the defect. The conduction band width reflects the degree of the charge localization*

Oxide	Lattice	Charge localized on defect neighboring atoms (%)	Relative orbital contributions for cations nearest to defect (%)			Conduction band width (eV)
			s	*p*	*d*	
CdO	Rocksalt	18	79	3	18	1.55
In_2O_3	Byxbyite	31	81	8	11	1.41
h-ZnO	Wurtzite	39	45	16	39	0.96
c-ZnO	Rocksalt	27	64	8	28	1.16
β-Ga_2O_3	Monoclinic	61	56	33	11	0.45
α-Ga_2O_3	Corundum	53	66	21	13	0.65
CaO	Rocksalt	80	22	22	56	0.06
MgO	Rocksalt	85	29	47	24	0.16
Al_2O_3	Corundum	87	30	47	23	0.14

(Table 1.6). Due to the high anisotropy of the *p* and *d* orbitals, strong covalent M-O bonds are formed near the oxygen defect. The resulting charge confinement is clearly seen from the charge density plots for oxygen-deficient MgO and CaO (Figure 1.10). This is not the case for rocksalt ZnO where the *s* state contributions are more than two times larger (Table 1.6).

A comparison of the electronic band structure of stoichiometric undoped MgO, CaO and Al_2O_3 (Figure 1.9) with the one in the conventional TCOs (Figure 1.2), reveals that the fundamental differences in the electronic properties of these oxides originate from the different energy location of the metal's empty *p* or *d* states with respect to the conduction band bottom. In In_2O_3, SnO_2, CdO or ZnO, the metal *p* band is well above its *s* band (Figures 1.2 and 1.9). As a result, the charge transport occurs via the M*s*–O*p* network, even

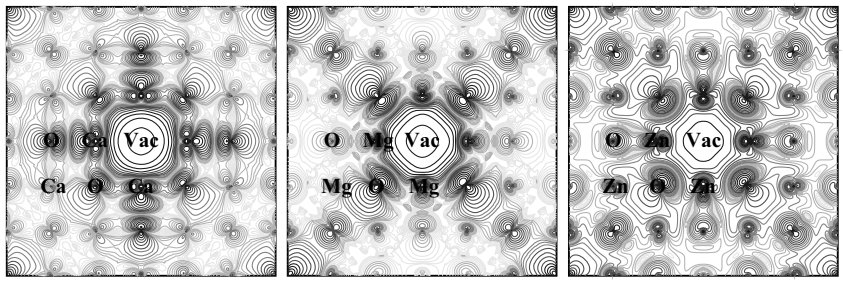

Figure 1.10 *Contour plots of the charge density distribution near the Fermi level in oxygen-deficient rocksalt CaO, MgO and ZnO. The charge confinement near the oxygen vacancy (an F-center defect) is clearly seen in CaO and MgO but not in ZnO where the charge distribution is more uniform*

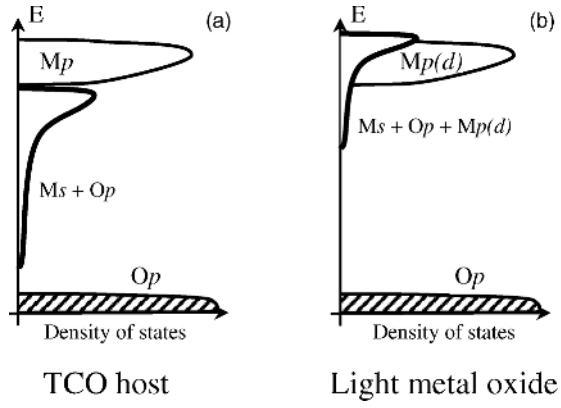

Figure 1.11 *Schematic electronic structure of main group metal oxides. (a) In conventional TCOs (post-transition metal oxides) Ms-type conduction band bottom ensures a uniform Ms–Op network for good carrier transport. (b) In oxides of lighter metals, e.g. Ga, Al, Mg or Ca, a substantial contribution from the metal anisotropic p or d states leads to a strong localization of doping-induced electrons*

for a large carrier concentration, i.e. when the BM shift is large. The spherical symmetry of the metal *s* orbitals and their strong hybridization with the *p* orbitals of the oxygen neighbors provides the most uniform charge distribution throughout the cell and, thus, facilitates good carrier transport.

In striking contrast to the conventional TCO hosts, in oxides of light metals the metal *p* or *d* bands almost coincide with its *s* band (Figures 1.9 and 1.11). When an oxygen vacancy is created, the Mg *p*, Al *p* or Ca *d* orbitals are energetically available for the induced electrons. Strong binding of these highly anisotropic orbitals with the states of the nearest oxygen atoms lowers the total energy of the system. The charge confinement explains the large formation energy of the oxygen vacancy in these refractory oxides as compared with the conventional TCOs where extra electrons are delocalized. Likewise, charge trapping on the anisotropic *p* or *d* states is expected for other carrier generation mechanisms, e.g. substitutional doping.

Naturally, the transition between the conventional TCO hosts (CdO, ZnO, In_2O_3 and SnO_2) and classic insulators (e.g. CaO and Al_2O_3) is not abrupt. The proximity of the metal *p* or *d* states to the *s*-type conduction band bottom in oxide of a main group metal (with ns^2 electronic configuration) will determine the orbital composition of the conduction band wavefunction. As an example, in oxygen-deficient β-Ga_2O_3, about 50% of the total cation contributions to the conduction band wavefunction comes from the Ga atoms nearest to the oxygen defect – to be compared with the same result for In_2O_3 (21%) on one side and Al_2O_3 (81%) or CaO (85%) on the other. Consistent with the degree of electron localization near the vacancy site, the conduction band width is smallest in CaO, MgO and Al_2O_3 followed gradually by Ga_2O_3, ZnO, In_2O_3 and CdO (Table 1.6). The second gap which splits this lowest conduction band from the higher band is found to be 3.80 eV in Al_2O_3, 1.44 eV in Ga_2O_3, 0.79 eV in ZnO, 0.64 eV in In_2O_3 and 0.20 eV in CdO, which also correlates with the degree of the electron binding.

The above band structure considerations generalize the fundamental physical properties in the main group metal oxides and also suggest ways to overcome the electron localization in these materials which we consider below.

1.7 Carrier Delocalization in Complex Oxides

The analysis in the previous section suggests a way to facilitate electrical charge transport in an oxide of main group metal(s) – via reduction of the contributions from the cation(s) *p* or *d* states at the energies near the Fermi level.

In Ga_2O_3, the Ga *p* band is located relatively close to the metal *s* band but does not coincide with it exactly as, for example, in Al_2O_3 (Figure 1.9). This leads to considerable but not dominant contributions from the Ga *p* states near the bottom of the conduction band. Hence, in Ga_2O_3, alternative carrier generation may give satisfactory results. For example, doping with a transition metal ion is expected to lead to a smaller BM shift associated with filling of the localized *d* states of the *d*-metal impurity (see Section 1.4). This would help to keep the detrimental Ga *p* states at energies high enough to make them unavailable for the induced carriers.

The above approach of circumventing carrier localization in Ga_2O_3 will not be successful in CaO or Al_2O_3 where the metal *s* and *p* or *d* bands overlap significantly. In the latter case, the electronic structure of the hosts should be altered via band engineering to attain the desired M*s*–O*p* hybridized conduction state. This approach is considered below.

1.7.1 Multicomponent Oxides with Layered Structures

In Section 1.5, it was shown that layered multicomponent oxides have a hybrid conduction band which consists of the *s* states of all consituent cations including light metal ions (if any). Due to the interaction between the alternating metal and oxygen atoms, the band gap of the complex material is an effective average over those in the corresponding single-cation oxides. For example, the band gap of $InAlZnO_4$ (3.5 eV) or $InAlCaO_4$ (4.6 eV) is smaller than the one in CaO (7.2 eV) or Al_2O_3 (9.1 eV) and larger than the one in In_2O_3 or ZnO ($\sim$3.4 eV) (Tables 1.1 and 1.5). This suggests that the hybrid conduction band of complex oxides can be driven away from the Al *p* and Ca *d* states via proper material composition to reduce the contributions from these states detrimental for carrier transport near the Fermi level (Figure 1.12).

Electronic band structure calculations of undoped stoichiometric $InAlZnO_4$ and $InAlCaO_4$ [51] indeed confirm that the Al *p* and Ca *d* states are at least 3 eV above the bottom of the conduction band as compared with 1.5 eV in Al_2O_3 and –1.2 eV in CaO where the Ca *d* band is *below* its *s* band (Figure 1.9). Nonetheless, Ca and Al will participate in the charge transport – *by providing their states* for extra electrons once the latter fill the conduction band. This is confirmed by isotropic electronic properties found in oxygen-deficient $InAlZnO_4$ and $InAlCaO_4$ [51]. Despite the preferential distribution of the oxygen vacancies which tend to concentrate in the $InO_{1.5}$ layer, the contributions to the conduction band wave function from different layers are comparable (Table 1.7) and the electron velocities calculated within and across the layers have similar values (Table 1.7). We note here that the electron velocity values for these oxides, although reduced, are comparable with

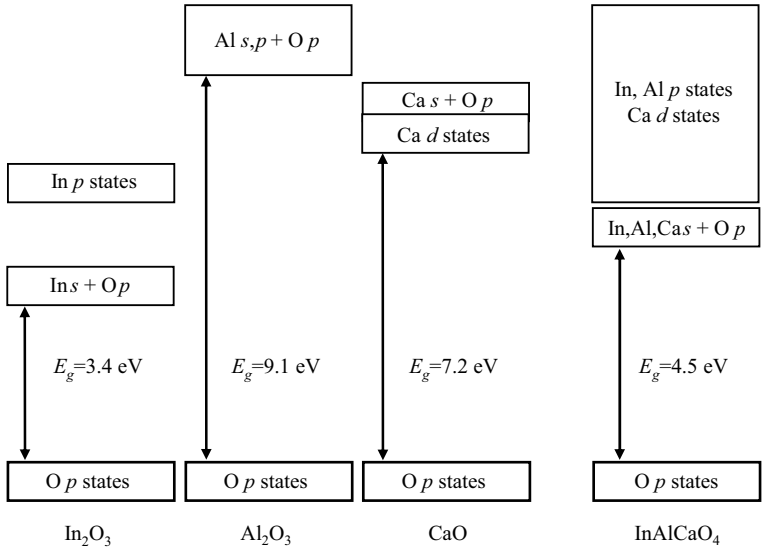

Figure 1.12 *Hybrid nature of the conduction band in single and multi-cation TCO hosts which consists primarily of the cation s states and the p states of oxygen atoms (see also Figures 1.1, 1.2, 1.9 and 1.11). Due to the band gap averaging, the conduction band in $InAlCaO_4$ is displaced away from the empty Al p and Ca d states to form a three-dimensional Ms–Op network for transport of extra electrons which fill the band upon doping*

those calculated for oxygen-deficient $InGaZnO_4$ which has been successfully employed as a TCO [36, 37, 69].

To summarize, multicomponent oxides offer a possibility to overcome the electron localization effects by tuning their electronic properties via proper composition. We stress, that both the relative content of the constituent oxides as well as their band gaps are crucial parameters that control the resulting optical and transport properties. For example, larger Al_2O_3 content in a multicomponent oxide where other constituents possess smaller band gaps, e.g. ZnO and In_2O_3, will result in an increase of the band

Table 1.7 *Net contributions from the states of the atoms that belong to the InO1 or Y_2O2 layers (Y = Zn, Al and/or Ca) to the conduction band wavefunction near Γ point, in per cent; and the Fermi electron group velocity v, in $\times 10^{-5}$ m s^{-1}, calculated along the specified crystallographic directions for oxygen-deficient layered oxides*

InY_2O_4	Contributions				Electron velocity		
	N_{In}	N_{O1}	N_{Y2}	N_{O2}	$v_{[100]}$	$v_{[010]}$	$v_{[001]}$
$InAlZnO_4$	27	37	13	23	3.1	3.3	3.4
$InAlCaO_4$	35	45	9	11	3.0	3.2	3.1
$InGaZnO_4$	24	32	21	23	3.8	4.0	4.6

gap. This may be appealing from the optical properties standpoint; it would also allow optimization of the oxide work function desired for a specific application. However, larger Al_2O_3 content with respect to the other constituents will also effectively move the hybrid conduction band closer to the Al *p* states, increasing their contributions and limiting the charge transport via an increased electron localization. This, along with the challenges of carrier generation in multicomponent oxides outlined in Section 1.5, suggests that careful microscopic analysis is required to produce a viable complex TCO.

1.7.2 Nanoporous Calcium Aluminate

In 2002, a persistent conductivity with a 10-order of magnitude change (from 10^{-10} to $\sim 1\,S\,cm^{-1}$) has been observed in $12CaO{\cdot}7Al_2O_3$ upon H doping followed by UV irradiation [73, 74]. Currently, conductivities as high as $1700\,S\,cm^{-1}$ have been achieved and various conversion approaches – in addition to photoactivation – have been developed [75–82].

$12CaO \cdot 7Al_2O_3$ or mayenite, a member of Portland cements, has a unique zeolite-like crystal structure with spacious cages of about 5.6 Å in diameter [83]. The cage framework includes 32 of the oxygen atoms in the unit cell while the remaining O^{2-} ion, which provides charge neutrality, is located inside one of the six cages. These encaged oxygen ions are loosely bound to the cage walls and can be easily substituted [84, 85] or reduced [76, 80, 81]. Indeed, our calculated formation energy of the oxygen vacancy in $12CaO \cdot 7Al_2O_3$ is 8–10 eV lower than those in the oxygen-deficient CaO or Al_2O_3 [50].

It has been shown that the nanoporous structure of $12CaO{\cdot}7Al_2O_3$ results in the formation of the so-called cage (or cavity) conduction band (CCB) [86, 87]. It consists of five bands (Figure 1.13) associated with the five empty cages in the unit cell. The sixth

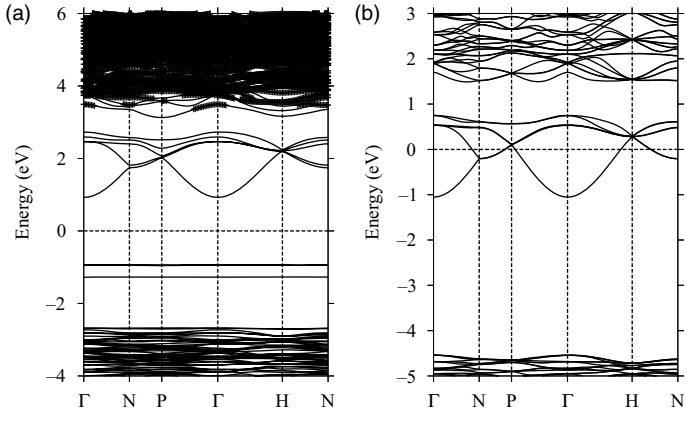

Figure 1.13 *Electronic band structure of (a) stoichiometric undoped and (b) oxygen-deficient $12CaO \cdot 7Al_2O_3$. In (a) the Ca d and Al p states are highlighted with (+) symbols. The encaged loosely bound O^{2-} ions give rise to the occupied flatbands below the Fermi level, cf. (a). When these O^{2-} are removed, cf. (b), the Fermi level shifts up into the cage conduction band formed by the Ca s and O p states giving rise to high electrical conductivity*

cage is filled with O^{2-} giving rise to the fully occupied flatbands (p_x, p_y, p_z) below the Fermi level. Due to the presence of the encaged oxygen ions, the CCB is shifted into the lower energy region and is located well below the framework conduction band (Figure 1.13). Most importantly, it was found that the latter is composed of the Ca *d* and Al *p* states. Hence, these orbitals will not be available to the vacancy-induced electrons, even if all the encaged oxygen ions are removed (which corresponds to the extra electron concentration of 2.33×10^{21} cm^{-3} and to the Fermi level shift of ~1.0 eV counting from the bottom of the CCB).

The analysis of the nature of the CCB in oxygen reduced $12CaO{\cdot}7Al_2O_3$ suggests that the conduction wave function is composed primarily of the Ca *s* and O *p* states (46% and 48% of the total charge in the cell, respectively). Since all Ca atoms in the cell give identical contributions to the conduction band, the resulting charge density distribution is uniform throughout the cage framework. The delocalization of the extra electrons in the reduced $12CaO{\cdot}7Al_2O_3$ [88] manifests itself in a large electron velocity (5.57×10^{-5} m s^{-1} in the [111] direction) to be compared with those calculated for oxygen deficient In_2O_3 (5.88×10^{-5} m s^{-1}) and ZnO (3.90×10^{-5} m s^{-1}) with similar electron concentration.

Another advantage of the unique crystal structure of $12CaO{\cdot}7Al_2O_3$ is that the CCB consists of six bands (Figure 1.13). They appear due to the six cages in a single unit cell of this material. Due to the uniform charge distribution throughout all cages [88], the lowest conduction state does not split off when oxygen vacancy is created. Therefore, oxygen reduction in $12CaO{\cdot}7Al_2O_3$ leads to two carriers per vacancy – in marked contrast to the conventional TCOs where the $V_O^{\bullet\bullet}$ defect leads to the completely occupied single conduction state being split from the rest of the band and only an excited or partially compensated vacancy can lead to conducting behavior (see Section 1.3.2).

Thus, the unusual nanoporous structure of $12CaO{\cdot}7Al_2O_3$ and the presence of the encaged O^{2-} ions result in the formation of the M*s*–O*p* hybridized conduction band located well below the detrimental Ca *d* and Al *p* orbitals. This explains the observed insulator-to-metal transition and the high electrical conductivity in oxygen-reduced $12CaO{\cdot}7Al_2O_3$ [76, 80–82].

1.8 An Outlook: Toward an Ideal TCO

Despite the success of converting the wide band gap $12CaO{\cdot}7Al_2O_3$ into a conductor via oxygen reduction, the conversion process resulted in a greatly increased absorption [76] making it inferior in relation to the conventional TCOs. The absorption arises due to optical transitions E_i within the CCB, which has width of 1.8 eV, as well as the transitions E_c from the Fermi level into the empty framework conduction band which have energies throughout the entire visible range (Figure 1.13). Importantly, band structure analysis suggests that nanoporous $12CaO{\cdot}7Al_2O_3$ belongs to a conceptually new class of transparent conductors [12]. In striking contrast to the conventional TCOs, where there is an unavoidable trade-off between optical absorption and conductivity, nanoporous materials offer a possibility to combine a complete, i.e. 100%, optical transparency with high electrical conductivity.

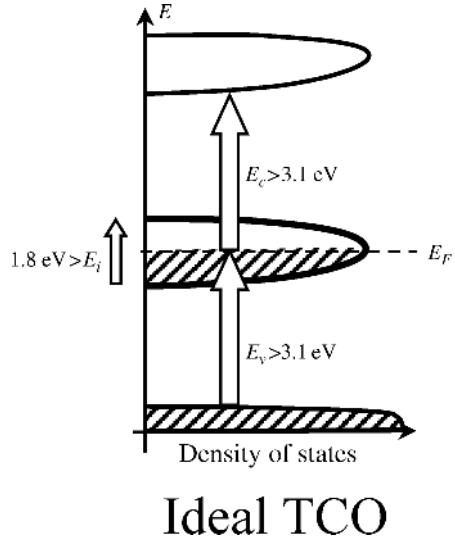

Figure 1.14 *Schematic electronic band structure of an ideal TCO*

The schematic band structure of the proposed [12] 'ideal' TCO is depicted in Figure 1.14. Introduction of a deep 'impurity' band with a high density of states (crossed by the Fermi level to make the system conducting) in the band gap of an insulating host material would help to keep intense inter-band transitions (from the valence band to the impurity band, E_v, and from the impurity band to the conduction band, E_c) above the visible range. This requires the band gap of a host material to be more than 6.2 eV. In addition, the impurity band should be narrow enough (<1.8 eV) to keep intra-band transitions E_i as well as the plasma frequency below the visible range [12]. To achieve high conductivity, the concentration of impurities should be high enough so that their electronic wave functions overlap well to form a *band*. The formation of the band would lead to a high carrier mobility due to the extended nature of these states and a relatively low scattering.

To fabricate such an ideal TCO, a material with a close-packed structure may not be suitable, because the required large concentration of impurities would result in: (i) an increase of ionized impurity scattering which limits electron transport; and (ii) a large structural relaxation in the host material, affecting its electronic structure and, most likely, decreasing the desired optical transparency. These effects are, indeed, observed in conventional TCOs (cf. Section 1.3).

Alternatively, materials with a nanoporous structure may offer a way to incorporate a large concentration of impurities into the pores without any significant changes in the band structure of the host material. Zeolites have been proposed [12] as potential candidates for such ideal TCOs. This class of materials possesses the desired structural and optical features, namely, spacious interconnected pores and large band gaps, as well as exhibit the ability to trap functional 'guest' atoms inside the nanometer-sized cavities which would govern the transport properties of the material.

In conclusion, understanding the principles of the conventional transparent conductors provides a solid foundation for further search of novel TCO host materials as well as efficient carrier generation mechanisms to make them good conductors. *Ab initio* density-functional band structure investigations are instrumental not only in providing a thorough insight into the TCO basics but also in predicting hidden capabilities of the materials beyond those traditionally employed.

Acknowledgements

The author acknowledges the support by the National Science Foundation and by the Petroleum Research Fund of the American Chemical Society. Computational resources for this work were provided by the San Diego Supercomputer Center (SDSC) supported by the National Science Foundation and National Energy Research Scientific Computing Center (NERSC) supported by the Department of Energy.

References

[1] K. L. Chopra, S. Major and D. K. Pandya, Transparent conductors – a status review, *Thin Solid Films*, **102**, 1–46 (1983).
[2] A. L. Dawar and J. C. Joshi, Semiconducting transparent thin films: their properties and applications, *J. Mater. Sci.*, **19**, 1–23 (1984).
[3] H. L. Hartnagel, A. L. Dawar, A. K. Jain and C. Jagadish, *Semiconducting Transparent Thin Films*, Institute of Physics Publishing, London, 1995.
[4] D. S. Ginley and C. Bright (Editors), Special issue on Transparent Conducting Oxides, *MRS Bull.*, **25**, (2000).
[5] E. Fortunato, D. Ginley, H. Hosono and D. C. Paine, Transparent conducting oxides for photovoltaics, *MRS Bull.*, **32**, 242–247 (2007).
[6] G. J. Exarhos and X.-D. Zhou, Discovery-based design of transparent conducting oxide films, *Thin Solid Films*, **515**, 7025–7052 (2007).
[7] J. C. C. Fan and J. B. Goodenough, X-ray photoemission spectroscopy studies of Sn-doped indium-oxide films, *J. Appl. Phys.*, **48**, 3524–3531 (1977).
[8] A. J. Freeman, K. R. Poeppelmeier, T. O. Mason, R. P. H. Chang and T. J. Marks, Chemical and thin-film strategies for new transparent conducting oxides, *MRS Bull.*, **25**, 45–51 (2000).
[9] O. N. Mryasov and A. J. Freeman, Electronic band structure of indium tin oxide and criteria for transparent conducting behavior, *Phys. Rev. B*, **64**, 233 111 (2001).
[10] R. Asahi, A. Wang, J. R. Babcock, N. L. Edleman, A. W. Metz, M. A. Lane, V. P. Dravid, C. R. Kannewurf, A. J. Freeman and T. J. Marks, First-principles calculations for understanding high conductivity and optical transparency in $In_xCd_{1-x}O$ films, *Thin Solid Films*, **411**, 101–105 (2002).
[11] H. Mizoguchi and P. M. Woodward, Electronic structure studies of main group oxides possessing edge-sharing octahedra: implications for the design of transparent conducting oxides, *Chem. Mater.*, **16**, 5233–5248 (2004).
[12] J. E. Medvedeva and A. J. Freeman, Combining high conductivity with complete optical transparency: a band-structure approach, *Europhys. Lett.*, **69**, 583–587 (2005).
[13] J. E. Medvedeva, Unconventional approaches to combine optical transparency with electrical conductivity, *Appl. Phys. A*, **89**, 43–47 (2007).
[14] E. Burstein, Anomalous optical absorption limit in InSb, *Phys. Rev.*, **93**, 632–633 (1954).
[15] T. S. Moss, The interpretation of the properties of indium antimonide, *Proc. Phys. Soc. B*, **67**, 775–782 (1954).

[16] J. R. Bellingham, W. A. Phillips and C. J. Adkins, Intrinsic performance limits in transparent conducting oxides, *J. Mater. Sci. Lett.*, **11**, 263–265 (1992).
[17] T. J. Coutts, D. L. Young and X. Li, Characterization of transparent conducting oxides, *MRS Bull.*, **25**, 58–65 (2000).
[18] G. Frank and H. Köstlin, Electrical properties and defect model of tin-doped indium oxide layers, *Appl. Phys. A*, **27**, 197–206 (1982).
[19] Highly precise all-electron full-potential linearized augmented plane wave (FLAPW) method [20, 21] within the local density approximation (LDA) and the screened-exchange LDA [22–24] was employed for the electronic band structure investigations.
[20] E. Wimmer, H. Krakauer, M. Weinert and A. J. Freeman, Full-potential self-consistent linearized-augmented-plane-wave method for calculating the electronic structure of molecules and surfaces – O_2 molecule, *Phys. Rev. B*, **24**, 864–875 (1981).
[21] M. Weinert, E. Wimmer and A. J. Freeman, Total-energy all-electron density functional method for bulk solids and surfaces, *Phys. Rev. B*, **26**, 4571–4578 (1982).
[22] D. M. Bylander and L. Kleinman, Good semiconductor band gaps with a modified local-density approximation, *Phys. Rev. B*, **41**, 7868–7871 (1990).
[23] A. Seidl, A. Görling, P. Vogl, J. A. Majewski and M. Levy, Generalized Kohn-Sham schemes and the band-gap problem, *Phys. Rev. B*, **53**, 3764–3774 (1996).
[24] R. Asahi, W. Mannstadt and A. J. Freeman, Optical properties and electronic structures of semiconductors with screened-exchange LDA, *Phys. Rev. B*, **59**, 7486–7492 (1999).
[25] R. L. Weiher and R. P. Ley, Optical properties of indium oxide, *J. Appl. Phys.*, **37**, 299–302 (1966).
[26] I. Hamberg, C. G. Granqvist, K. F. Berggren, B. E. Sernelius and L. Engström, Band-gap widening in heavily Sn-doped In_2O_3, *Phys. Rev. B*, **30**, 3240–3249 (1984).
[27] F. P. Koffyberg, Thermoreflectance spectra of CdO: band gaps and band-population effects, *Phys. Rev. B*, **13**, 4470–4476 (1976).
[28] C. Kligshirn, The luminescence of ZnO under high one- and two-quantum excitation, *Phys. Status Solidi B*, **71**, 547 (1975).
[29] D. Fröhlich, R. Kenklies and R. Helbig, Band-gap assignment in SnO_2 by two-photon spectroscopy, *Phys. Rev. Lett.*, **41**, 1750–1751 (1978).
[30] N. W. Ashcroft and N. D. Mermin, *Solid State Physics*, W.B. Saunders, Philadelphia, 1976.
[31] J. E. Medvedeva, Averaging of the electron effective mass in multicomponent transparent conducting oxides, *Europhys. Lett.*, **78**, 57 004 (2007).
[32] J. E. Medvedeva, E. N. Teasley and M. D. Hoffman, Electronic band structure and carrier effective mass in calcium aluminates, *Phys. Rev. B*, **76**, 155 107 (2007).
[33] H. Hosono, Ionic amorphous oxide semiconductors: material design, carrier transport, and device application, *J. Non-Cryst. Solids*, **352**, 851 (2006).
[34] A. J. Leenheer, J. D. Perkins, M. F. A. M. van Hest, J. J. Berry, R. P. O'Hayre and D. S. Ginley, General mobility and carrier concentration relationship in transparent amorphous indium zinc oxide films, *Phys. Rev. B*, **77**, 115 215 (2008).
[35] K. Nomura, T. Kamiya, H. Ohta, T. Uruga, M. Hirano and H. Hosono, Local coordination structure and electronic structure of the large electron mobility amorphous oxide semiconductor In-Ga-Zn-O: experiment and ab initio calculations, *Phys. Rev. B*, **75**, 035 212 (2007).
[36] K. Nomura, H. Ohta, A. Takagi, T. Kamiya, M. Hirano and H. Hosono, Room temperature fabrication of transparent flexible thin-film transistors using amorphous oxide semiconductors, *Nature*, **432**, 488–492 (2004).
[37] K. Nomura, H. Ohta, K. Ueda, T. Kamiya, M. Hirano and H. Hosono, Thin-film transistor fabricated in single-crystalline transparent oxide semiconductor, *Science*, **300**, 1269–1272 (2003).
[38] K. J. Button, C. G. Fonstad and W. Dreybrodt, Determination of the electron masses in stannic oxide by submillimeter cyclotron resonance, *Phys. Rev. B*, **4**, 4539–4542 (1971).
[39] T. Minami, New n-type transparent conducting oxides, *MRS Bull.*, **25**, 38–43 (2000).
[40] S. Jin, Y. Yang, J. E. Medvedeva, J. R. Ireland, A. W. Metz, J. Ni, C. R. Kannewurf, A. J. Freeman and T. J. Marks, Dopant ion size and electronic structure effects on transparent

conducting oxides. Sc-doped CdO thin films grown by MOCVD, *J. Am. Chem. Soc.*, **126**, 13 787–13 793 (2004).
[41] Y. Yang, S. Jin, J. E. Medvedeva, J. R. Ireland, A. W. Metz, J. Ni, M. C. Hersam, A. J. Freeman and T. J. Marks, CdO as the archetypical transparent conducting oxide. Systematics of dopant ionic radius and electronic structure effects on charge transport and band structure, *J. Am. Chem. Soc.*, **127**, 8796–8804 (2005).
[42] S. Jin, Y. Yang, J. E. Medvedeva, L. Wang, S. Li, N. Cortes, J. R. Ireland, A. W. Metz, J. Ni, M. C. Hersam, A. J. Freeman and T. J. Marks, Tuning the properties of transparent oxide conductors. Dopant ion size and electronic structure effects on CdO-based transparent conducting oxides. Ga- and In-doped CdO thin films grown by MOCVD, *Chem. Mater.*, **20**, 220–230 (2008).
[43] L. Vegard, Die Konstitution der Mischkristalle und die Raumfullung der Atome, *Z. Phys.*, **5**, 17–26 (1921).
[44] L. V. Morozova and A. V. Komarov, Solid solutions based on cadmium oxide in the CdO-In_2O_3 system, *Russ. J. Appl. Chem.*, **68**, 1240–1242 (1995).
[45] Y. Dou, R. G. Egdell, T. Walker, D. S. L. Law and G. Beamson, N-type doping in CdO ceramics: a study by EELS and photoemission spectroscopy, *Surf. Sci.*, **398**, 241–258 (1998).
[46] T. B. Reed, *Free Energy of Formation of Binary Compounds*, MIT Press, Cambridge, MA, 1971.
[47] J. H. W. de Wit, G. van Unen and M. Lahey, Electron concentration and mobility in In_2O_3, *J. Phys. Chem. Solids*, **38**, 819–824 (1977).
[48] F. A. Kröger, *The Chemistry of Imperfect Crystals*, North-Holland, Amsterdam, 1974.
[49] S. Lany and A. Zunger, Dopability, intrinsic conductivity and nonstoichiometry of transparent conducting oxides, *Phys. Rev. Lett.*, **98**, 045 501 (2007).
[50] J. E. Medvedeva and C. L. Hettiarachchi, Tuning the properties of complex transparent conducting oxides: role of crystal symmetry, chemical composition and carrier generation, to be published in, *Phys. Rev. B.*
[51] J. E. Medvedeva,Toward conductive main group metal oxides: overcoming electron localization, to be published.
[52] I. Tanaka, K. Tatsumi, M. Nakano and H. Adachi, First-principles calculations of anion vacancies in oxides and nitrides, *J. Am. Ceram. Soc.*, **85**, 68–74 (2002).
[53] Ç. Kiliç and A. Zunger, Origins of coexistence of conductivity and transparency in SnO_2, *Phys. Rev. Lett.*, **88**, 95 501 (2002).
[54] J. E. Medvedeva, Magnetically mediated transparent conductors: In_2O_3 doped with Mo, *Phys. Rev. Lett.*, **97**, 086 401 (2006).
[55] Y. Meng, X. Yang, H. Chen, J. Shen, Y. Jiang, Z. Zhang and Z. Hua, A new transparent conductive thin film In_2O_3:Mo, *Thin Solid Films*, **394**, 219–223 (2001).
[56] Y. Yoshida, D. M. Wood, T. A. Gessert and T. J. Coutts, High-mobility sputtered films of indium oxide doped with molybdenum, *Appl. Phys. Lett.*, **84**, 2097–2099 (2004).
[57] S. Sun, J. Huang and D. Lii, Effects of oxygen contents on the electrical and optical properties of indium molybdenum oxide films fabricated by high density plasma evaporation, *J. Vac. Sci. Technol. A*, **22**, 1235–1239 (2004).
[58] R. D. Shannon, J. L. Gillson and R. J. Bouchard, Single crystal synthesis and electrical properties of $CdSnO_3$, Cd_2SnO_4, In_2TeO_6, $CdIn_2O_4$, *J. Phys. Chem. Solids*, **38**, 877–881 (1977).
[59] H. Kawazoe and K. Ueda, Transparent conducting oxides based on the spinel structure, *J. Am. Ceram. Soc.*, **82**, 3330–3336 (1999).
[60] B. J. Ingram, G. B. Gonzalez, D. R. Kammler, M. I. Bertoni and T. O. Mason, Chemical and structural factors governing transparent conductivity in oxides, *J. Electroceram.*, **13**, 167–175 (2004).
[61] H. Un'no, N. Hikuma, T. Omata, N. Ueda, T. Hashimoto and H. Kawazoe, *Jpn. J. Appl. Phys.*, **32**, L1260–L1262 (1993).
[62] J. M. Phillips, J. Kwo and G. A. Thomas, Transparent conducting thin films of $GaInO_3$, *Appl. Phys. Lett.*, **65**, 115–117 (1994).

[63] H. Hiramatsu, H. Ohta, W. S. Seo and K. J. Koumoto, Thermoelectric properties of $(ZnO)_5In_2O_3$ thin films prepared by r.f. sputtering method, *J. Jpn. Soc. Powder Powder Metall.*, **44**, 44–49 (1997).
[64] H. Kaga, R. Asahi and T. Tani, Thermoelectric properties of highly textured Ca-doped (ZnO)(m) In_2O_3 ceramics, *Jpn. J. Appl. Phys.*, **43**, 7133–7136 (2004).
[65] M. Orita, H. Ohta, M. Hirano, S. Narushima and H. Hosono, Amorphous transparent conductive oxide $InGaO_3(ZnO)_m$ ($m \leq 4$): a Zn 4s conductor, *Phil. Mag. B*, **81**, 501–515 (2001).
[66] M. Orita, M. Takeuchi, H. Sakai and H. Tanji, New transparent conductive oxides with $YbFe_2O_4$ structure, *Jpn. J. Appl. Phys.*, **34**, L1550–L1552 (1995).
[67] K. Von Kato, I. Kawada, N. Kimizuka and T. Katsura Die Kristallstructur von $YbFe_2O_4$, *Z. Krist.*, **141**, 314–320 (1975).
[68] N. Kimizuka and T. Mohri, Spinel, $YbFe_2O_4$, and $Yb_2Fe_3O_7$ types of structures for compounds in the In_2O_3 and Sc_2O_3-A_2O_3-BO systems [A: Fe, Ga or Al; B: Mg, Mn, Fe, Ni, Cu or Zn] at temperatures over 1000 °C, *J. Solid State Chem.*, **60**, 382–384 (1985).
[69] N. Kimizuka and T. Mohri, Structural classification of $RAO_3(MO)_n$ compounds (R = Sc,In,Y or lanthanides; A = Fe(III), Ga, Cr, or Al; M = Divalent Cation; n = 1–11), *J. Solid State Chem.*, **78**, 98–107 (1989).
[70] G. F. Neumark, Defects in wide band gap II–VI crystals, *Mater. Sci. Eng. R*, **21**, 1–46 (1997).
[71] C. G. Van de Walle, Strategies for controlling the conductivity of wide-band-gap semiconductors, *Phys. Status Solidi B*, **229**, 221–228 (2002).
[72] A. Zunger, Practical doping principles, *Appl. Phys. Lett.*, **83**, 57–59 (2003).
[73] K. Hayashi, S. Matsuishi, T. Kamiya, M. Hirano and H. Hosono, Light-induced conversion of an insulating refractory oxide into a persistent conductor, *Nature*, **419**, 462–465 (2002).
[74] J. E. Medvedeva, A. J. Freeman, M. I. Bertoni and T. O. Mason, Electronic structure and light-induced conductivity in a transparent refractory oxide, *Phys. Rev. Lett.*, **93**, 16 408 (2004).
[75] Y. Toda, S. Matsuishi, K. Hayashi, K. Ueda, T. Kamiya, M. Hirano and H. Hosono, Field emission of electron anions clathrated in subnanometer-sized cages in $[Ca_{24}Al_{28}O_{64}]^{4+}$ ($4e^-$), *Adv. Mater.*, **16**, 685–689 (2004).
[76] S. Matsuishi, Y. Toda, M. Miyakawa, K. Hayashi, T. Kamiya, M. Hirano, I. Tanaka and H. Hosono, High-density electron anions in a nanoporous single crystal: $[Ca_{24}Al_{28}O_{64}]^{4+}$ ($4e^-$), *Science*, **301**, 626–629 (2003).
[77] S. W. Kim, M. Miyakawa, K. Hayashi, T. Sakai, M. Hirano and H. Hosono, Simple and efficient fabrication of room temperature stable electride: melt-solidification and glass ceramics, *J. Am. Chem. Soc.*, **127**, 1370–1371 (2005).
[78] S. W. Kim, Y. Toda, K. Hayashi, M. Hirano and H. Hosono, Synthesis of a room temperature stable 12CaO·7Al(2)O(3) electride from the melt and its application as an electron field emitter, *Chem. Mater.*, **18**, 1938–1944 (2006).
[79] S. W. Kim, K. Hayashi, M. Hirano, H. Hosono and I. Tanaka, Electron carrier generation in a refractory oxide 12CaO·7Al(2)O(3) by heating in reducing atmosphere: conversion from an insulator to a persistent conductor, *J. Am. Ceram. Soc.*, **89**, 3294–3298 (2006).
[80] S. W. Kim, S. Matsuishi, T. Nomura, Y. Kubota, M. Takata, K. Hayashi, T. Kamiya, M. Hirano and H. Hosono, Metallic state in a lime-alumina compound with nanoporous structure, *Nano Lett.*, **7**, 1138–1143 (2007).
[81] M. Bertoni, PhD Thesis, Northwestern University, Evanston, IL, 2006.
[82] M. Bertoni, J. Medvedeva, Y. Q. Wang, A. Freeman, K. R. Poeppelmeier and T. Mason, Enhanced electronic conductivity in Si-substituted calcium aluminate, *J. Appl. Phys.*, **102**, 113 704 (2007).
[83] A. N. Christensen, Neutron powder diffraction profile refinement studies on Ca11.3Al14O32.3 and CaClO(D0.88H0.12), *Acta Chem. Scandinavica*, **A41**, 110–112 (1987).
[84] J. Jeevaratnam, F. P. Glasser and L. S. Dent Glasser, Anion substitution and structure of $12CaO.7Al_2O_3$, *J. Am. Ceram. Soc.*, **47**, 105–106 (1964).
[85] G. I. Zhmoidin and G. S. Smirnov, Characteristics of the crystals of derivatives of $12CaO{\cdot}7Al_2O_3$, *Inorganic Mater.*, **18**, 1595–1601 (1982).

[86] P. V. Sushko, A. L. Shluger, K. Hayashi, M. Hirano and H. Hosono, Hopping and optical absorption of electrons in nano-porous crystal $12CaO{\cdot}7Al_2O_3$, *Thin Solid Films*, **445**, 161–167 (2003).
[87] Z. Y. Li, J. L. Yang, J. G. Hou and Q. S. Zhu, Is mayenite without clathrated oxygen in inorganic electride?, *Angew. Chem., Int. Ed.*, **43**, 6479–6482 (2004).
[88] J. E. Medvedeva and A. J. Freeman, Hopping versus bulk conductivity in transparent oxides: $12CaO{\cdot}7Al_2O_3$, *Appl. Phys. Lett.*, **85**, 955–957 (2004).